

Investigations of nonlinear femtosecond pulse propagation with the inclusion of Raman, shock, and third-order phase effects

Alex A. Zozulya,¹ Scott A. Diddams,² and Tracy S. Clement²

¹*Department of Physics, Worcester Polytechnic Institute, 100 Institute Road, Worcester, Massachusetts 01609-2280*

²*JILA, University of Colorado and National Institute of Standards and Technology, Boulder, Colorado 80309-0440*

(Received 20 January 1998; revised manuscript received 30 March 1998)

The propagation of intense femtosecond pulses in a nonlinear, dispersive bulk medium is investigated numerically in the regime where the combined effects of diffraction, normal dispersion, and cubic nonlinearity lead to pulse splitting. We present numerical solutions of a modified (3+1)-dimensional nonlinear Schrödinger equation, accounting for the Raman effect, linear and nonlinear shock terms, third-order dispersion, and initial temporal third-order phase modulation. The calculated results are found to be in good agreement with experimental measurements. [S1050-2947(98)04410-2]

PACS number(s): 42.65.Re, 42.65.Jx, 42.65.Sf

I. INTRODUCTION

The advent of intense femtosecond laser pulses has introduced challenging propagation-related problems with important implications for atmospheric propagation [1,2], laser-plasma interactions [3,4], and optical switching [5]. Many aspects of femtosecond pulse propagation are adequately explained by the standard (3+1)-dimensional nonlinear Schrödinger equation (NLSE), which accounts for diffraction, group velocity dispersion (GVD), and an instantaneous Kerr nonlinearity [6]. However, as peak powers increase and pulse widths decrease, the standard NLSE begins to fail and details surrounding the pulse propagation are less known. It has been shown that near or below a certain threshold power, GVD is sufficient to arrest the collapse of the field to a singularity [7]. However, in the standard NLSE the strength of the nonlinear term scales as $1/d^3$ (d being the characteristic diameter of the pulse in space and time), while the linear dispersion and diffraction scale as $1/d^2$. The mathematical implication is that with increasing input power, the nonlinear terms will ultimately dominate the linear terms and push the field towards a singularity. The physical reality is different and experimental observations in different solids and gases at high powers do not indicate that catastrophic beam collapse occurs [8,9]. The conclusion must be that at higher powers the standard NLSE does not fully describe the situation at hand and therefore it is important to consider the individual and combined contributions of higher-order modifying terms of the NLSE.

Knowing what additional physical mechanisms must be included in the theoretical description and verifying the subsequent numerical predictions with experimental data are two challenging tasks. Not only is the problem computationally expensive, but accurate measurements are difficult due to the complex spectral, spatial, and temporal variations in the electric field. The approach taken here is to slowly push forward the theoretical description, adding contributions of various physical processes as they become important. Along these lines, we consider the manifestations of the Raman nonlinearity, shock terms, and third-order phase effects in

the normal dispersion regime of bulk media where femtosecond pulse splitting has recently been predicted [7,10–15] and observed [16–18]. In particular, we focus on effects that lead to recently observed asymmetries in the pulse splitting [17,18]. Using parameters typical of the normal dispersion regime of fused silica, we find that the dynamics are mainly determined by the shock terms and the Raman nonlinearity, with third-order dispersion (TOD) and an initial third-order temporal phase modulation playing secondary roles. The numerical predictions are found to be in good agreement with experimental results, which are also presented.

II. THEORETICAL MODEL

Assuming a complex field of the form $E(\vec{r}, z, t) = a(\vec{r}, z, t) \exp(ikz - i\omega_0 t)$, the evolution of the slowly varying, complex envelope $a(\vec{r}, z, t)$ can be modeled with the modified nonlinear Schrödinger equation [7,11–13,16,18,19]

$$i \frac{\partial}{\partial z} a + \left(1 + i \epsilon_\omega \frac{\partial}{\partial t} \right)^{-1} \nabla^2 a - \frac{\partial^2}{\partial t^2} a - i \epsilon_3 \frac{\partial^3}{\partial t^3} a + N_{nl} \left(1 + i \epsilon_\omega \frac{\partial}{\partial t} \right) g a = 0. \quad (1)$$

Equation (1) is written using normalized variables in the coordinate frame moving at the group velocity of the pulse. The temporal, longitudinal, and transverse coordinates are normalized to the characteristic pulse duration τ , the dispersion length $l_D = 2\tau^2/k''$, and the characteristic transverse length $l_\perp = \sqrt{l_D/2k}$, respectively. The parameter $N_{nl} = 2\pi n_2 l_D |a_0|^2 / \lambda$ is the normalized nonlinearity, with n_2 being the nonlinear index of refraction and $|a_0|^2$ the characteristic intensity. In addition, $\epsilon_\omega = 1/\omega_0 \tau$ and $\epsilon_3 = k'''/3k''\tau$. In these definitions, $k = 2\pi n/\lambda$, where n is the linear index of refraction at the central wavelength λ . The dispersion coefficients k'' and k''' are the second and third derivatives of k with respect to frequency, both evaluated at the central frequency ω_0 . The transverse Laplacian $\nabla^2 = \partial^2/\partial r^2 + \partial/r\partial r$ accounts for diffraction, while the second and third time de-

rivatives describe GVD and TOD, respectively. Space-time focusing in Eq. (1) is accounted for by the time derivative in the term $[1 + i\epsilon_\omega(\partial/\partial t)]^{-1}\nabla^2 a \approx [1 - i\epsilon_\omega(\partial/\partial t)]\nabla^2 a$ and by a part of the nonlinear shock term $N_{nl}\epsilon_\omega\partial(ga)/\partial t$. In the original formulation of Rothenberg [20], it was given by the cross term $\epsilon_\omega\partial^2 a/\partial z\partial t$, which is readily obtained from Eq. (1) when it is multiplied by the operator $[1 + i\epsilon_\omega(\partial/\partial t)]$. The space-time focusing accounts for the contribution to the group velocity (along the z axis) of an off-axis ray due to its nonzero angle with respect to the z axis. As implied by the functional form $\epsilon_\omega\partial/\partial t$, space-time focusing is similar to the *nonlinear* shock described by the time derivative in the last term of Eq. (1) [21]. For this reason, we will refer to the $\epsilon_\omega(\partial/\partial t)\nabla^2 a$ part of space-time focusing as being a *linear* shock term. The nonparaxiality term proportional to $\partial^2 a/\partial z^2$ has been neglected in Eq. (1) [22–24]. Its relative magnitude is determined by the parameter $\epsilon_k = 1/2kl_D \ll 1$. In the range of parameters investigated below, the contribution of this term turns out to be small.

It is well known that the nonlinear susceptibility of transparent optical glasses is comprised of a near-instantaneous electronic response in addition to a delayed inertial response [25]. In the nonlinear terms of Eq. (1), we account for both the instantaneous and noninstantaneous nonlinearities using the model proposed in Refs. [26,27]:

$$g = (1 - \alpha)|a(t)|^2 + \alpha \int_{-\infty}^t d\tau f(t - \tau)|a(\tau)|^2, \quad (2)$$

where the response function f is approximated by the relation

$$f(t) = \frac{1 + (\omega_r\tau_r)^2}{\omega_r\tau_r^2} \exp(-t/\tau_r)\sin(\omega_r t). \quad (3)$$

The delayed response, also called the Raman response, is due to vibrations of the nuclei that are excited by the optically induced (fast) perturbation of the electronic structure. In Eq. (2), α denotes the fractional amount of time-delayed Raman response, whereas the instantaneous part of the response is proportional to $1 - \alpha$. For fused silica we use $\alpha = 0.15$, $\tau_r = 50$ fs for the characteristic Raman response time, and $\omega_r\tau_r = 4.2$ [25–27]. We note that in the limit of $\tau \gg \tau_r$, Eq. (2) can be reduced to

$$g = |a(t)|^2 - T_r \frac{\partial |a(t)|^2}{\partial t}, \quad (4)$$

where $T_r = \alpha 2\tau_r/[1 + (\omega_r\tau_r)^2]$. In all numerical simulations that we present, the full form of the Raman nonlinearity [Eqs. (2) and (3)] has been employed. As will be discussed later, the simplified expression of Eq. (4) is used only to check the results in limiting situations.

Variations of Eq. (1) have been studied previously. Numerical analysis of Eq. (1) with $\epsilon_\omega = \epsilon_3 = 0$ and the assumption of an instantaneous nonlinearity has been undertaken in Refs. [7,10–12,14,15]. In this situation, it was found that normal dispersion (NGVD; such that $k'' > 0$) can result in pulse splitting and in some cases is sufficient to halt the critical collapse of the self-focused field. As already noted, the space-time focusing term was included by Rothenberg

[12] and has recently been studied in combination with the nonlinear shock term, here again assuming an instantaneous nonlinearity [18,19]. Manassah and Gross [13,28] included TOD, Raman nonlinearity, and nonlinear shock in their numerical studies. However, their works neglected the linear contribution $\epsilon_\omega(\partial/\partial t)\nabla^2 a$ from space-time focusing. For propagation in water and air, the effects of ionization have also been considered [4,29], but here again space-time focusing was not included. As will be shown in the following, all of the terms included in Eq. (1) are significant in the regime of interest and therefore should not be neglected.

Unless noted, all simulations use parameters typical of recent pulse-splitting experiments in fused silica [17]. The initial field is taken to be a Gaussian in both time and space, having an intensity full width at half maximum (FWHM) of 90 fs and 70 μm , respectively [30]. The beam waist is located at the entrance face of the sample. The center wavelength is $\lambda = 0.8 \mu\text{m}$ and if not explicitly stated, the peak intensity of the input is $I_{\text{pk}} = 85 \text{ GW/cm}^2$. The linear index of refraction is $n = 1.45$, the nonlinear index of refraction is $n_2 = 2.5 \times 10^{-16} \text{ GW/cm}^2$ [31,32] and the GVD and TOD coefficients are $k'' = 360 \text{ fs}^2/\text{cm}$ and $k''' = 275 \text{ fs}^3/\text{cm}$ [33]. Equation (1) is solved in cylindrical geometry using a symmetric split-step technique. For the linear part of each step, the time derivatives are evaluated in the frequency domain, while the transverse Laplacian is computed using finite differences with a five-point stencil. The time-dependent nonlinear part of the equation is also evaluated using the same finite-difference technique.

III. NUMERICAL RESULTS

Initially, we set $\epsilon_3 = \epsilon_\omega = \alpha = 0$ such that Eq. (1) contains only terms that describe (to lowest order) diffraction, dispersion, and an instantaneous Kerr nonlinearity. It is this standard form of the NLSE that was used to predict pulse splitting in normally dispersive media [10–12]. As a means of introducing the basic physical processes involved, we first present numerical solutions of this simplified equation, focusing on parameters that are pertinent to experiments in fused silica [17]. We then reintroduce the higher-order terms one at a time, emphasizing the physical significance each term brings to Eq. (1).

A. Self-focusing and symmetric pulse splitting

The results of numerical solutions of Eq. (1) with $\epsilon_3 = \epsilon_\omega = \alpha = 0$ are shown in Figs. 1 and 2. Figure 1 contains surface plots of the intensity profile $I(\vec{r}, t)$ at three different propagation lengths. For these simulations, the peak input intensity is set to $I_{\text{pk}} = 85 \text{ GW/cm}^2$, corresponding to $P_{\text{pk}} = I_{\text{pk}}\pi w_0^2/2 = 4.7 \text{ MW}$. This is 1.8 times the critical power for self-focusing given by $P_{\text{crit}} = (0.61\lambda_0)^2\pi/8n_0n_2 = 2.6 \text{ MW}$. Steady-state, paraxial approximations predict a collapse of the field to a singularity after about 1.7 cm of propagation under these conditions [34]. However, as seen in both Figs. 1 and 2, the pulse smoothly passes through a focus with no collapse, although temporal splitting is observed. In this situation, the combined action of NGVD and self-phase modulation (SPM) are sufficient to arrest the collapse by spreading the pulse energy in time, thereby reducing the

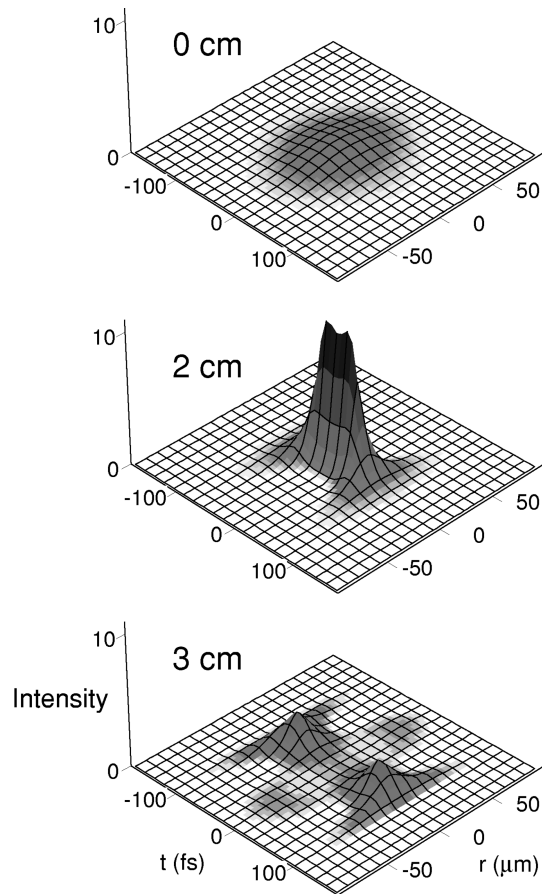


FIG. 1. Calculated surface plots of the intensity profile $I(\vec{r}, t)$ of an intense femtosecond pulse propagating in fused silica. The three plots correspond to the positions of $z=0, 2,$ and 3 cm, respectively. The intensity scale is normalized by 85 GW/cm^2 , which is the peak intensity at $z=0$ cm. The radial and temporal units on all three plots are the same, being micrometers and femtoseconds, respectively.

peak intensity [7,8]. We note, however, that this is not generally the case as the input power is increased further. An interesting feature seen in the plot at $z=3$ cm of Fig. 1 is the presence of energy that is radiated outward (along the radius) at $t=0$. The two small pulses centered at $r \approx \pm 60 \mu\text{m}$ have peak intensities that are 7% of the peak intensities of the two pulses located at $r=0 \mu\text{m}$.

The evolution of the propagation seen in Fig. 1 is summarized in Fig. 2, where we plot the spatial and temporal FWHM and the peak intensity for the field. Figure 2(a) shows the time-integrated spatial FWHM of the intensity. Similarly, Fig. 2(b) shows the on-axis ($r=0$) temporal FWHM of the pulse, where the solid line is the FWHM of the entire intensity structure and the dotted line is the FWHM of the individual split pulses. As seen in Fig. 1, the splitting is symmetric such that both leading and trailing pulses are identical. Figure 2(c) shows the peak intensity of the field, where once again the intensities of the leading and trailing pulses are identical after splitting occurs. From these data we see that the field undergoes strong self-focusing with the time-integrated spatial FWHM decreasing from the initial $70 \mu\text{m}$ to about $15 \mu\text{m}$. As the pulse focuses spatially, its on-axis temporal width actually decreases by close to 50%. This is the temporal pulse sharpening predicted and mea-

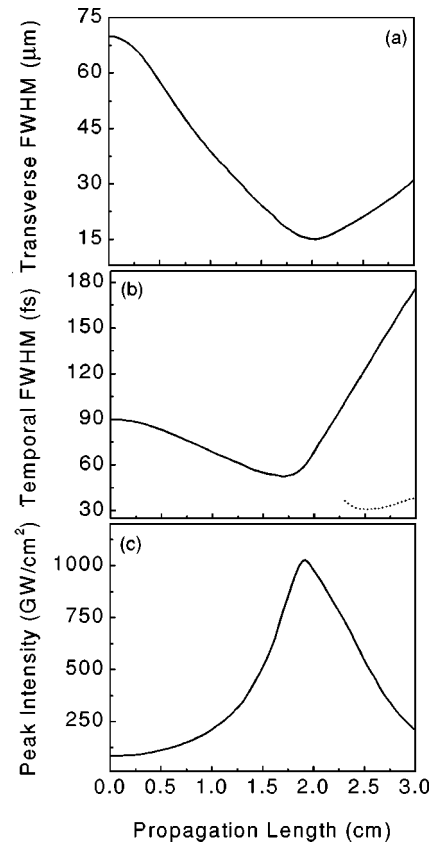


FIG. 2. (a) Calculated time-integrated spatial FWHM of the intensity, (b) calculated on-axis temporal FWHM of the intensity, and (c) calculated peak intensity of a femtosecond pulse propagating in fused silica. In (b) the solid line is the FWHM of the entire intensity profile, while the dotted line is the FWHM of the individual split pulses.

sured 30 years ago [35,36]. Near the position $z=1.75$ cm, the pulse stops focusing temporally and at $z=2.3$ cm the pulse is split to the extent that the FWHM of the two sub-pulses may be measured. It is at this point that we see the start of the dotted line in Fig. 2(b), with the individual split pulses each having a FWHM on the order of 35 fs. These trends are reflected in Fig. 2(c), where the peak intensity (always on axis in this case) is plotted as a function of the same propagation distance. Figure 2(a) demonstrates that the approximately 13 times increase in intensity is primarily due to the strong self-focusing rather than the reduction in pulse width.

From a simple physical standpoint, we understand the process of pulse splitting as follows. Initially, self-focusing moves off-axis energy towards the peak of the pulse and compresses it in both space and time [35]. As the peak intensity increases, the process of SPM also increases, thereby generating new frequency components. The combination of the SPM-induced upchirp and NGVD then acts to push the energy away from $t=0$, initiating the pulse splitting. As this process continues, the peak intensity drops, stopping the collapse at $t=0$. However, off-axis energy continues to focus at $t \neq 0$ such that two pulses are resolved [12]. Although additional physical effects will be considered in the following sections, the effects of self-focusing, SPM, and NGVD remain the key elements of the femtosecond pulse propagation presented throughout this work.

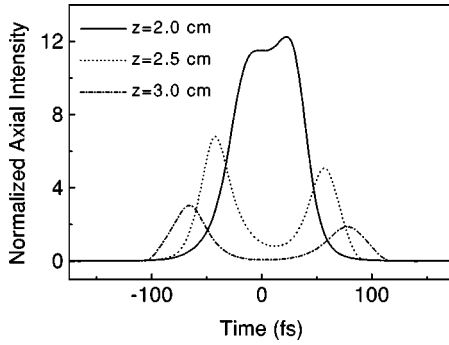


FIG. 3. Calculated on-axis intensity profile of split pulses with the inclusion of the Raman effect. The three different curves are the intensity profiles at the corresponding propagation distances shown in the legend. The intensity axis is normalized by the peak input intensity, which is 85 GW/cm^2 .

B. Inclusion of the Raman effect

The principle change due to the inclusion of the Raman effect ($\alpha \neq 0$, $\epsilon_3 = \epsilon_\omega = 0$) is the asymmetry between the leading and trailing pulses. This is seen in Fig. 3, where the on-axis intensity profile of the pulse is plotted at three different values of the propagation distance z . Here we see that for the position $z=3.0 \text{ cm}$, the leading pulse has close to 1.5 times the peak intensity of the trailing pulse. The increase of the leading pulse at the expense of the trailing pulse can be understood simply in terms of Raman gain. Indeed, the response function of Eq. (3) is the time-domain representation of the more common frequency-domain picture of stimulated Raman scattering, whereby redshifted frequency components are amplified at the expense of the blueshifted components. Stimulated Raman scattering occurs before the pulse splits and because NGVD moves the red components ahead of the blue components, it follows that the leading pulse ends up larger [13].

Similar to the previous case with no Raman contribution, during the first 1.5 cm of propagation, the field is first compressed temporally by about 30% before it begins to split. An interesting point seen in Fig. 3 is that when the pulse first begins to split at $z=2.0 \text{ cm}$, the trailing peak has a higher intensity than the leading peak. This trend rapidly reverses and the leading pulse maintains a higher peak intensity for propagation distances greater than $z \sim 2.25 \text{ cm}$. Additional simulations using the nonlinearity of Eq. (4) result in the leading peak being larger than the trailing peak for all propagation distances. This leads us to conclude that the presence of the more intense trailing peak, as seen at $z=2.0 \text{ cm}$ in Fig. 3, is a consequence of the pulse width and the Raman response time being of the same order in these simulations.

The shifting of energy from high to low frequencies is seen in the on-axis spectra shown in Fig. 4. These spectra are obtained from the Fourier transform of the field used to calculate the time-domain intensity profiles shown in Fig. 3. For reference, the spectrum of the input field ($z=0$) has also been included and all spectra in the figure are normalized by the peak spectral intensity of this input. In addition, the somewhat arbitrary center frequency is given by $\nu_0 = c/\lambda$, where c is the speed of light and $\lambda = 0.8 \mu\text{m}$. Accompanying the shift to low frequency, we also see significant spectral broadening due to SPM and spectral modulation at the ex-

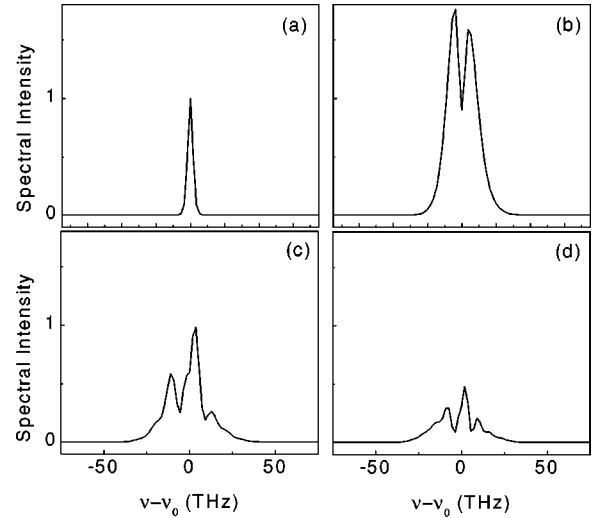


FIG. 4. Calculated on-axis spectral intensity of a femtosecond pulse propagating in bulk fused silica with the inclusion of the Raman effect. The four plots are the spectra at the propagation distances of (a) $z=0 \text{ cm}$, (b) $z=2 \text{ cm}$, (c) $z=2.5 \text{ cm}$, and (d) $z=3 \text{ cm}$. The intensity axes are normalized by the peak spectral intensity of the input ($z=0 \text{ cm}$).

pected frequency of $\nu_m \sim 2/T$, where T is the time domain separation of the split pulses. It is also evident that between $z=2.5$ and $z=3 \text{ cm}$ there is mainly a decrease in the on-axis spectral intensity, but little change in the shape of the spectrum. This indicates that after 2.5 cm of propagation, the field has passed through the focus and nonlinear effects have become less important.

C. Shock terms

With $\epsilon_\omega \neq 0$, $\epsilon_3 = \alpha = 0$, just shock terms are included in Eq. (1). The predominant effect of these terms is highlighted in Fig. 5, where the on-axis intensity profile is plotted at successive propagation lengths. For Fig. 5(a), just the *nonlinear* shock term of Eq. (1) is included. Here again, pulse splitting is clearly seen, but in this situation, the trailing pulse is larger than the leading pulse during the splitting process. This results from the nonlinear increase in the index of refraction at the peak of the pulse and the resulting decrease in the group velocity of the peak relative to the lower-intensity parts of the pulse. Thus the peak of the pulse lags behind the lower-intensity parts, leading to shock formation at the trailing edge [21]. The shock formation is clearly evident in the profiles at $z=2.0, 2.25$, and 2.5 cm , which show the trailing edge of the pulse to be much sharper than the leading edge. One also notes that the entire field is delayed in time relative to $t=0$, further evidence of intensity-dependent group delay. Although the shock formation initially results in a much larger trailing pulse, Fig. 5(a) also demonstrates that the relative amplitudes of the two pulses reverse by $z=3.0 \text{ cm}$ of propagation such that the leading pulse is larger. This reversal results from the fact that unless it is continuously compressed, the trailing pulse (with its higher intensity and shorter duration) will spread much faster than the longer and lower-intensity leading pulse.

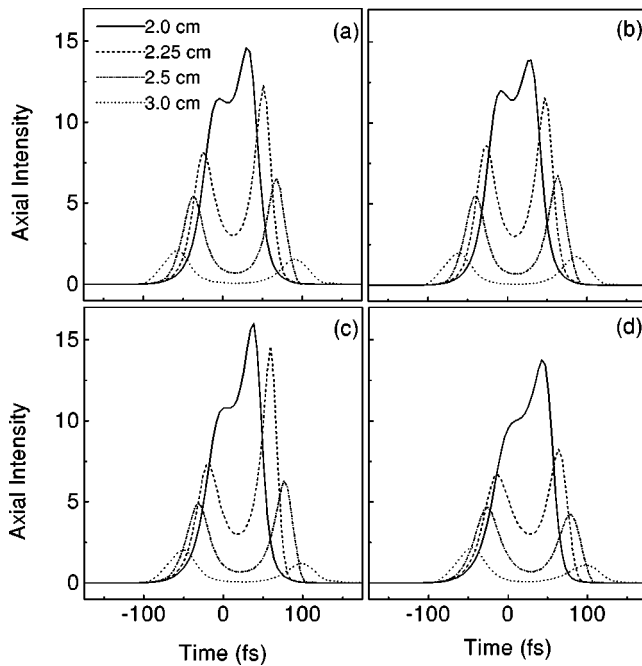


FIG. 5. Calculated on-axis intensity profile of split pulses with the inclusion of (a) just nonlinear shock, (b) just linear shock (space-time focusing), (c) both nonlinear and linear shock terms, and (d) both shock terms plus Raman effects. The different curves are the intensity profiles at the corresponding propagation distances shown in the legend. The intensity axes are normalized by the peak input intensity and the legend of (a) applies to all plots.

Space-time focusing has a similar effect as shown in Fig. 5(b), where just the *linear* shock term of Eq. (1) has been included. In this case, however, the shift of energy to later times is the result of the significant increase of the angular spectrum of the pulse as it passes through the nonlinear focus. A comparison of Figs. 5(a) and 5(b) shows that the individual contributions of the linear and nonlinear shock terms are similar and of the same order. This is evidence of the importance of keeping both of these terms in Eq. (1), as was done for the result of Fig. 5(c). As shown, the combination of the linear and nonlinear shock terms results in further enhancement of the trailing peak.

The result of the inclusion of the Raman effect along with both shock terms is summarized in Fig. 5(d) and illustrated in the surface plots of Fig. 6. In Fig. 5(d) we see that the Raman effect (with its amplification of the leading pulse) acts to dampen the shock effects, but does not completely counterbalance them. For example, the profiles in Fig. 5(d) at $z=2.0$ and $z=2.25$ cm are lower in intensity and lack the very sharp trailing edge seen in Fig. 5(c). However, in Figs. 5(a)–5(d) the trailing pulse always remains larger during the splitting process. This is in contrast to the situation already presented in Fig. 3, where the Raman effect acting alone always results in a larger leading pulse. These features are illustrated in the surface plots of Fig. 6. Here we see the increase in peak intensity by about a factor of 12, along with the shock formation that leads first to the growth of the trailing peak ($z=2.0$ and 2.25 cm) and then its rapid decrease after passing through the focus ($z=3$ cm). As in Fig. 1, there is evidence of energy being radiated outward in the radial direction from near the central temporal position of the field.

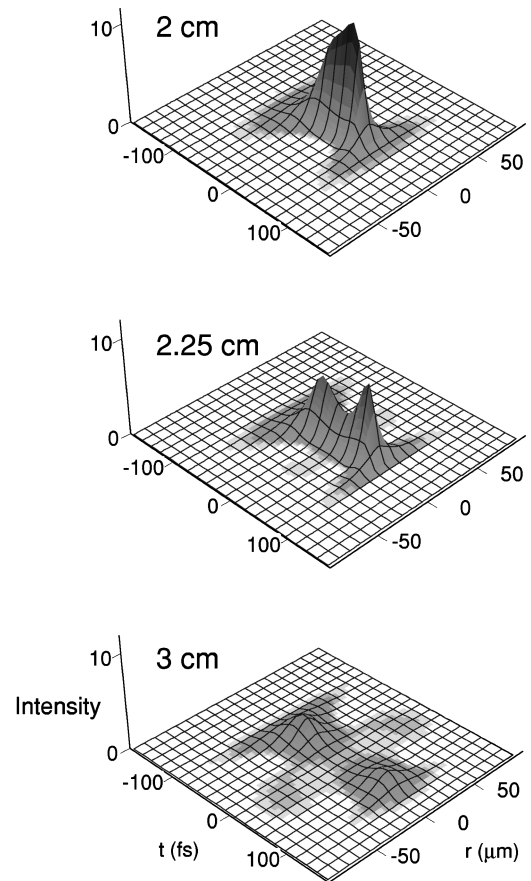


FIG. 6. Calculated surface plots of the intensity profile $I(\vec{r}, t)$ of an intense femtosecond pulse propagating in fused silica with the inclusion of both Raman and shock effects. The three plots correspond to the positions of $z=2$, 2.25 , and 3 cm, respectively. The intensity scale is normalized by 85 GW/cm^2 , which is the peak intensity at $z=0$ cm (see Fig. 1). The radial and temporal units on all three plots are the same, being micrometers and femtoseconds, respectively.

However, in this case, we see that the radiated energy lags towards the trailing pulse.

It is instructive here to also consider the frequency content of the split pulses. Figure 7(a) contains the Fourier transform of the on-axis field at $z=3.0$ cm with the shock and Raman terms included in Eq. (1). This is the Fourier transform of the field that has the temporal intensity profile shown previously in Fig. 5(d). In addition, the spectra of just the leading and trailing pulses are shown for comparison in Fig. 7(b). These spectra were obtained by cutting the time-domain data at the minimum intensity between the two pulses and then Fourier transforming these two independent fields. The results show clearly that the leading pulse is redshifted with respect to the trailing pulse and that the shock formation results in a long tail on the high-frequency side of the spectrum. It is these blue spectral components that are generated at the sharp trailing edge of the pulse seen in previous figures. In addition, Fig. 7 shows that much of the oscillatory structure in the spectrum of the full field is not present in the independent spectra of the leading and trailing pulses. In fact, the spectra of the leading and trailing pulses are quite smooth. This demonstrates that the structure in the

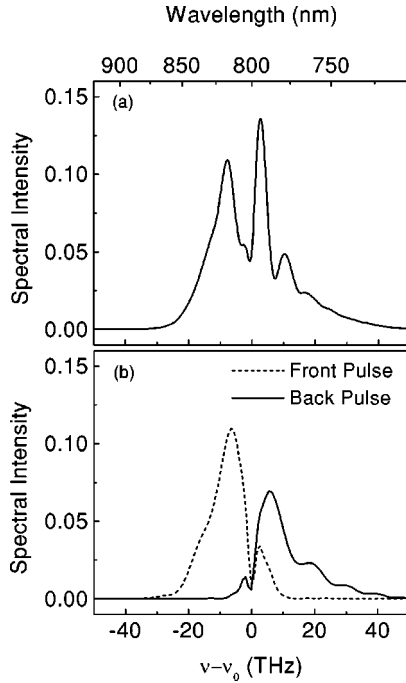


FIG. 7. (a) Calculated on-axis spectrum of a femtosecond pulse after propagation in fused silica. The corresponding temporal intensity profile is shown in Fig. 5(d). (b) The individual spectra of the front pulse (broken line) and the back pulse (solid line). All spectra are calculated after $z = 3.0$ cm of propagation with the inclusion of shock terms and the Raman effect.

spectrum of the full field is due to interferences between the two constituent pulses.

Figure 8 provides an alternative look at the frequency content of the split pulses. Here we plot the same on-axis intensity profile that was shown in Fig. 5(d) ($z = 3$ cm). In addition, we also present the corresponding on-axis instantaneous frequency, which is proportional to the first derivative of the temporal phase

$$\omega_{\text{inst}} = \omega_0 - \frac{\partial \phi}{\partial t}. \quad (5)$$

It is clear in Fig. 8 that the instantaneous frequency of leading pulse is predominantly redshifted with respect to the car-

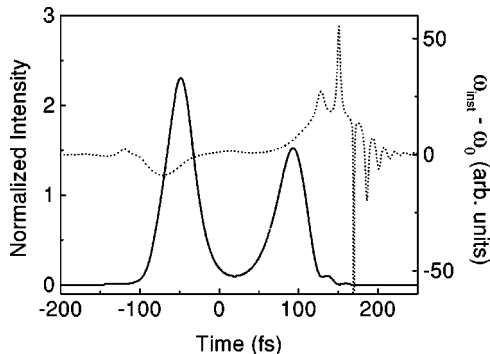


FIG. 8. Calculated on-axis intensity (solid line, left axis) and corresponding instantaneous frequency (dotted line, right axis) of an intense femtosecond pulse after $z = 3$ cm of propagation in fused silica.

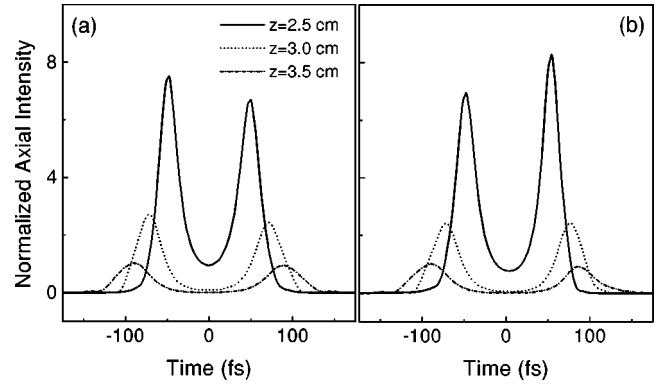


FIG. 9. Calculated on-axis intensity profiles for pulse splitting with (a) the inclusion of third-order dispersion and (b) the inclusion of positive third-order temporal phase modulation on the input field. The legend applies to both plots and in both cases Raman and shock effects are not included.

rier (ω_0), while the trailing pulse is largely blueshifted. To a good approximation, the instantaneous frequency also shows that both pulses have a predominantly positive linear chirp across their most intense regions. The large oscillations at the back edge of the trailing pulse are evidence of optical wavebreaking [37]. This is the result of the blueshifted peak of the field over running and interfering with the light in the tail of the pulse.

D. Spectral and temporal third-order phase effects

The final effects that we consider are the influence of third-order material dispersion and third-order temporal phase modulation on the input field. In this case, we set $\alpha = 0$ and eliminate the shock terms in Eq. (1). Third-order material dispersion is known to play an increasing role in femtosecond pulse propagation as the bandwidth of the pulse exceeds a few percent of the carrier frequency. As already mentioned, TOD is included in Eq. (1) in the term proportional to $\partial^3/\partial t^3$. In the normal dispersion regime of fused silica, the effect of TOD is to increase the GVD on the blue side of the spectrum, while decreasing the GVD on the red side of the spectrum. As might be expected in the regime of pulse splitting, this leads to more rapid spreading of the trailing (blue) pulse and therefore a decrease in the intensity of this pulse. This is shown in Fig. 9(a). Additional simulations show that when combined with the Raman effect, TOD tends to increase the intensity of the leading pulse and when combined with shock effects TOD acts to decrease the intensity of the trailing pulse. However, in both situations, the Raman and shock effects remain dominant over contributions from TOD.

With $\epsilon_3 = \epsilon_\omega = \alpha = 0$ in Eq. (1), the addition of third-order temporal phase modulation to the input field of the form $\phi(t) = ip(t/\tau)^3$ also results in asymmetry between the leading and trailing pulses. However, in this case the relative amplitude of the two pulses depends on the sign of p . Figure 9(b) shows the situation for $p = +0.1$. During the initial splitting, the trailing pulse is larger in this case, but similar to the results of Fig. 6 the more intense pulse spreads more rapidly so that at $z = 3.5$ cm the trailing pulse is larger. Results for $p = -0.1$ are exactly the opposite of those shown in

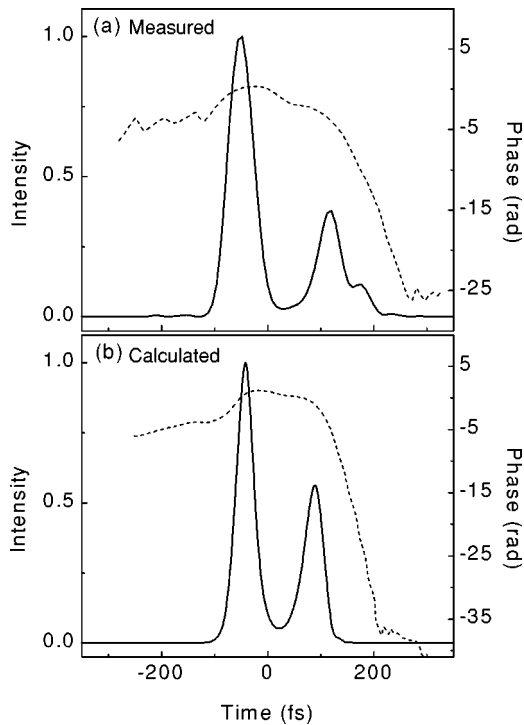


FIG. 10. (a) Measured and (b) calculated on-axis intensity (solid line) and phase (dashed line) of an intense femtosecond pulse after propagating through 3.0 cm of fused silica.

Fig. 9(b). Additional simulations in which shock and Raman effects are also included indicate that for reasonable experimental parameters [i.e., $p(t/\tau)^3 < 0.4$ rad across the FWHM of the pulse], the influence of third-order temporal phase modulation is small compared to the Raman and shock effects.

IV. COMPARISON WITH EXPERIMENT AND CONCLUSIONS

Finally, we make some comparison of these numerical calculations to experimental measurements. Both the time- and frequency-domain features presented in the previous sections are evident in the data of Figs. 10 and 11. Figure 10 shows the measured and calculated on-axis temporal intensity and phase of the complex pulse envelope after propagation through 3.0 cm of fused silica, while Fig. 11 shows the corresponding frequency-domain data. In short, the 800-nm output of a Ti:sapphire amplified laser system was spatially filtered and focused to a $75\text{-}\mu\text{m}$ waist (FWHM) at the entrance face of the fused silica. Temporally, the incident field was nearly bandwidth limited, with a duration of 90 fs (FWHM) and a peak power of 4.4 ± 0.4 MW. The measured temporal intensity and phase were obtained using frequency-resolved optical gating (FROG) [38], as described in greater detail elsewhere [17]. The measured spectrum of Fig. 11(a) was acquired with a 0.27-m grating spectrometer and a detector array. All data are averaged over several hundred laser pulses. The calculated curves of Figs. 10 and 11 use the full form of Eq. (1) with the previously given parameters of fused silica. The initial field is assumed to be a Gaussian (in space and time) having the measured beam parameters and a peak power of 4.9 MW. Good agreement exists between the

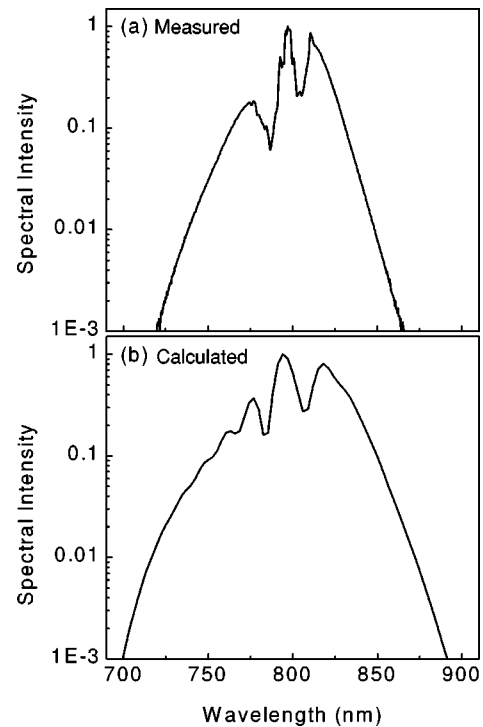


FIG. 11. (a) Measured and (b) calculated on-axis spectra corresponding to the time-domain data shown in Fig. 10.

measurements and the calculations in both time and frequency. As already highlighted in Fig. 5(d), after 3.0 cm of propagation the peak intensity of the trailing pulse has dropped below that of the leading pulse. Furthermore, the temporal phase provides additional details that remain ambiguous when only the intensity is known. For example, the overall negative curvature of the temporal phase indicates that the leading pulse is redshifted and the sharp drop in the phase along the back edge of the trailing pulse provides evidence of the shock formation in this same regime. In accordance with Eq. (5), this rapid phase variation gives rise to the longer blue spectral tail seen in both the measured and calculated spectra of Fig. 11. Our previous experimental results (with 2.54 cm of propagation) are also in qualitative agreement with the calculations of Fig. 5(d) [17]. In that case the trailing pulse was measured to be larger than the leading. In addition, we find our results to be in agreement with recent calculations and measurements of the power dependence (fixed sample length) of the pulse splitting process [18].

A notable discrepancy between the numerical and experimental results of Fig. 11 is found in the spectral widths of the field after propagation. This may be the result of a physical limit on the experimental transverse diameter of the self-focused pulse in the fused silica, which in turn yields lower intensities and less spectral broadening. Indeed, measurements of the spot size of the field exiting the sample indicate that it is larger than predicted theoretically [32]. Two possible explanations are aberrations (temporal and spatial) on the input field which limit the extent to which it can be self-focused or a higher-order mechanism, such as multiphoton ionization [4] or a saturating nonlinearity, which limits the maximum peak intensity. Currently, cross-section data for the necessary four- or five-photon absorption process in fused silica is unavailable, while recent measurements indi-

cate that any such nonlinear loss mechanism is small [18]. Additional simulations with slightly higher input intensities (90–100 GW/cm² with a 70- μ m spot size) indicate that the shock formation at the trailing edge of the field results in extensive spectral broadening toward the blue with peak intensities approaching 10 TW/cm². With such increasing intensities it may be that higher-order limiting terms must be included before further realistic predictions (of multiple splittings, for example [16,17]) will be obtained. We also note that the linear diffraction of the field from the output of the fused silica sample to the FROG measurement apparatus can result in modifications of the on-axis field. This issue and propagation at higher intensities will be discussed elsewhere.

In summary, we have numerically investigated the manifestations of Raman, linear shock (space-time focusing), nonlinear shock, and third-order phase effects on femtosecond pulse propagation in the regime where pulse splitting is observed. Of these three effects, the inclusion of shock terms

in the NLSE has the greatest influence, giving a sharp trailing edge to the field in the time domain and creating a blue-shifted spectral tail. To some extent, the Raman effect counterbalances the shock terms by shifting energy to the leading (redshifted) pulse. For reasonable experimental values, TOD and initial third-order phase modulation are found to be of the least consequence, although they do result in asymmetries in the split pulses. In the range of parameters investigated, nonparaxiality was determined to play an insignificant role and has not been included in any of the simulations. All calculations are shown to be in good agreement with experimental measurements.

ACKNOWLEDGMENTS

This work was supported in part by the National Science Foundation and the National Institute of Standards and Technology.

-
- [1] A. Braun *et al.*, *Opt. Lett.* **20**, 73 (1995).
 - [2] E. T. J. Nibbering *et al.*, *Opt. Lett.* **21**, 62 (1996).
 - [3] X. M. Zhao, J.-C. Diels, C. Y. Wang, and J. Elizondro, *IEEE J. Quantum Electron.* **31**, 599 (1995).
 - [4] Q. Feng *et al.*, *IEEE J. Quantum Electron.* **QE-33**, 127 (1997).
 - [5] R. McLeod, K. Wagner, and S. Blair, *Phys. Rev. A* **52**, 3254 (1995).
 - [6] J. H. Marburger, *Prog. Quantum Electron.* **4**, 35 (1975).
 - [7] G. G. Luther, J. V. Moloney, A. C. Newell, and E. M. Wright, *Opt. Lett.* **19**, 862 (1994).
 - [8] D. Strickland and P. B. Corkum, *J. Opt. Soc. Am. B* **11**, 492 (1994).
 - [9] D. von der Linde and H. Schüler, *J. Opt. Soc. Am. B* **13**, 216 (1996).
 - [10] N. A. Zharova *et al.*, *JETP Lett.* **44**, 13 (1986).
 - [11] P. Chernev and V. Petrov, *Opt. Lett.* **17**, 172 (1992).
 - [12] J. E. Rothenberg, *Opt. Lett.* **17**, 583 (1992).
 - [13] J. T. Manassah and B. Gross, *Laser Phys.* **6**, 563 (1996).
 - [14] B. Gross and J. T. Manassah, *Opt. Commun.* **126**, 269 (1996).
 - [15] M. Trippenbach and Y. B. Band, *Phys. Rev. A* **56**, 4242 (1997).
 - [16] J. K. Ranka, R. W. Schirmer, and A. L. Gaeta, *Phys. Rev. Lett.* **77**, 3783 (1996).
 - [17] S. A. Diddams, H. K. Eaton, A. A. Zozulya, and T. S. Clement, *Opt. Lett.* **23**, 379 (1998).
 - [18] J. K. Ranka and A. L. Gaeta, *Opt. Lett.* **23**, 534 (1998).
 - [19] T. Brabec and F. Krausz, *Phys. Rev. Lett.* **78**, 3282 (1997).
 - [20] J. Rothenberg, *Opt. Lett.* **17**, 1340 (1992).
 - [21] F. DeMartini, C. H. Townes, T. K. Gustafson, and P. L. Kelley, *Phys. Rev. Lett.* **164**, 312 (1967).
 - [22] M. D. Feit and J. A. Fleck, *J. Opt. Soc. Am. B* **5**, 633 (1988).
 - [23] G. Fibich, *Phys. Rev. Lett.* **76**, 4356 (1996).
 - [24] G. Fibich and G. C. Papanicolaou, *Opt. Lett.* **22**, 1379 (1997).
 - [25] R. Hellwarth, J. Cherlow, and T.-T. Yang, *Phys. Rev. B* **11**, 964 (1975).
 - [26] R. H. Stolen, J. P. Gordon, W. J. Tomlinson, and H. A. Haus, *J. Opt. Soc. Am. B* **6**, 1159 (1989).
 - [27] R. H. Stolen and W. J. Tomlinson, *J. Opt. Soc. Am. B* **9**, 565 (1992).
 - [28] J. T. Manassah and B. Gross, *Laser Phys.* **7**, 9 (1997).
 - [29] M. Mlejnek, E. M. Wright, and J. V. Moloney, *Opt. Lett.* **23**, 382 (1998).
 - [30] We have numerically verified that a hyperbolic secant temporal input yields qualitatively the same results as the Gaussian temporal input.
 - [31] A. J. Taylor, G. Rodriguez, and T. S. Clement, *Opt. Lett.* **21**, 1812 (1996).
 - [32] S. A. Diddams, H. K. Eaton, A. A. Zozulya, and T. S. Clement, *IEEE J. Sel. Top. Quantum Electron.* **4**, 306 (1998).
 - [33] S. Diddams and J.-C. Diels, *J. Opt. Soc. Am. B* **13**, 1120 (1996).
 - [34] R. W. Boyd, *Nonlinear Optics* (Academic, San Diego, 1992).
 - [35] J. H. Marburger and W. G. Wagner, *IEEE J. Quantum Electron.* **QE-3**, 415 (1967).
 - [36] G. L. McAllister, J. H. Marburger, and L. G. DeShazer, *Phys. Rev. Lett.* **21**, 1648 (1968).
 - [37] W. J. Tomlinson, R. H. Stolen, and A. M. Johnson, *Opt. Lett.* **10**, 457 (1985).
 - [38] R. Trebino *et al.*, *Rev. Sci. Instrum.* **68**, 3277 (1997). We note that there are two nonessential ambiguities in the FROG measurement: a constant phase factor and a constant time shift.